

# **Wiley Analytical Science Virtual Conference**

**November 9-17**



**For the 3rd time, The Wiley Analytical Science  
Conference is back!**

**It's all happening November 9 - 17**

The Wiley Analytical Science Virtual Conference will bring together thousands of researchers and practitioners to share current developments in science and industry. Join for exciting presentations from experts in the fields of analytical and bioanalytical chemistry, pharmaceutical research, materials science, lab automation, and related disciplines.

Register to learn about recent developments & applications in:

- Microscopy
- Spectroscopy
- Mass Spectrometry
- Separation Science
- Much more!

**Register here**

# Improving Perovskite Solar Cells: Insights From a Validated Device Model

Tejas S. Sherkar, Cristina Momblona, Lidón Gil-Escrig, Henk J. Bolink,  
and L. Jan Anton Koster\*

To improve the efficiency of existing perovskite solar cells (PSCs), a detailed understanding of the underlying device physics during their operation is essential. Here, a device model has been developed and validated that describes the operation of PSCs and quantitatively explains the role of contacts, the electron and hole transport layers, charge generation, drift and diffusion of charge carriers and recombination. The simulation to the experimental data of vacuum-deposited  $\text{CH}_3\text{NH}_3\text{PbI}_3$  solar cells over multiple thicknesses has been fit and the device behavior under different operating conditions has been studied to delineate the influence of the external bias, charge-carrier mobilities, energetic barriers for charge injection/extraction and, different recombination channels on the solar cell performance. By doing so, a unique set of material parameters and physical processes that describe these solar cells is identified. Trap-assisted recombination at material interfaces is the dominant recombination channel limiting device performance and passivation of traps increases the power conversion efficiency (PCE) of these devices by 40%. Finally, guidelines to increase their performance have been issued and it is shown that a PCE beyond 25% is within reach.

viz. mesoporous, planar, and inverted planar.<sup>[5,6]</sup> Planar device structures also offer the opportunity for fabrication of PSCs by vacuum evaporation in addition to the popular solution processing technique.<sup>[7–10]</sup> While PSCs have high power conversion efficiency (PCE), they are still far from their theoretical maximum (31%).<sup>[11]</sup> In order to propel them to their maximum theoretical efficiency, a basic understanding of the device physics of these solar cells is an essential first step.<sup>[12]</sup> A device model which can quantitatively explain the operation of PSCs can help identify areas for targeted improvement in performance.

Previous studies on device modeling of perovskite solar cells include a drift-diffusion model by Richardson et al. which focuses on extensively describing the current–voltage hysteresis phenomenon in perovskite solar cells by including the motion of ions.<sup>[13]</sup> Similarly, Van Reenen

et al. study the origin of hysteresis in perovskite solar cells.<sup>[14]</sup> The approach of Minemoto et al. is based on similarities with inorganic solar cells which is qualitative in nature.<sup>[15]</sup> Instead, we focus on devices with little or no hysteresis and achieve quantitative agreement with experimental data of highly reproducible perovskite solar cells, in turn delineating the role of all physical processes that describe the operation of these devices.

Typically, a perovskite solar cell is made up of a perovskite absorber layer sandwiched between the electron transport layer (ETL) and the hole transport layer (HTL). Light is absorbed in the perovskite layer which gives rise to free electrons and holes.<sup>[16]</sup> These free charge carriers then diffuse and drift under the influence of the electric field, with electrons moving toward the ETL and holes toward the HTL. The ETL and HTL are responsible for transporting the electrons and holes to respective electrodes for efficient extraction. Electrons and holes can also recombine in a radiative or non-radiative way which results in loss in device performance. A radiative recombination results from the annihilation of an electron in the conduction band (CB) and an hole in the valence band (VB) to emit a photon of energy equal to the band-gap ( $E_{\text{gap}}$ ) of the perovskite. On the other hand, nonradiative recombination takes place via an intermediate, such as a defect or a trap (an energy level in the band gap of the perovskite), occupied with either an electron or a hole (depending on the energy level of the trap) and an eventual annihilation with a hole in VB or electron in CB

## 1. Introduction

Photovoltaic cells based on thin-film technology are a viable source of affordable energy as they make use of much less material than their single-crystal counterparts which is directly related to the cost of production. Thin-film solar cells based on hybrid halide perovskites,  $\text{CH}_3\text{NH}_3\text{PbX}_3$  ( $\text{X} = \text{Cl}, \text{Br}, \text{I}$ ), are attracting great interest due to rapid increase in device efficiencies (now above 22%<sup>[1]</sup>) since their onset in 2008.<sup>[2]</sup> These materials have been shown to exhibit desirable properties for solar cell operation including direct band-gap, high absorption coefficient, high ambipolar charge mobilities, and long charge-carrier diffusion lengths.<sup>[2–4]</sup> These properties allows for perovskite solar cells (PSCs) to be prepared in various device architectures

T. S. Sherkar, Dr. L. J. A. Koster  
Zernike Institute for Advanced Materials  
University of Groningen  
Nijenborgh 4, 9747AG Groningen, The Netherlands  
E-mail: l.j.a.koster@rug.nl

C. Momblona, L. Gil-Escrig, Dr. H. J. Bolink  
Instituto de Ciencia Molecular  
Universidad de Valencia  
C/Catedrático J. Beltrán 2, 46980 Paterna (Valencia), Spain



DOI: 10.1002/aenm.201602432

respectively. Both radiative and nonradiative mechanisms are reported to exist in PSCs.<sup>[17–20]</sup> However, there are still many questions regarding the dominant recombination mechanism in PSCs and the processes limiting their performance, which are crucial for optimization.

In this paper, we explore ways to improve the efficiency of existing PSCs based on a planar device configuration. We achieve this by means of a validated device model which quantitatively explains the role of contacts, the electron and hole transport layers, charge generation, drift and diffusion of charge carriers and recombination. First a brief description of the model is presented, followed by an overview of relevant equations. Subsequently, simulation results are fit to the experimental data of vacuum-deposited  $\text{CH}_3\text{NH}_3\text{PbI}_3$  solar cells<sup>[21]</sup> over multiple absorber thicknesses showing the validity of our model. We present a detailed analysis of the device behavior delineating the influence of the external bias, charge-carrier mobilities, energetic barriers for charge injection/extraction, and different recombination channels on the solar cell performance. We identify trap-assisted recombination at the front interface (HTL/perovskite) as the dominant recombination channel limiting the performance of PSCs, with 22% of the free charge carriers lost at maximum power despite the high mobility of charge carriers in the perovskite. Finally, we issue guidelines for further improvement in the performance of PSCs, and show that PCE beyond 25% is within reach.

The experimental data presented in this paper is obtained from  $\text{CH}_3\text{NH}_3\text{PbI}_3$  solar cells with little hysteresis in their  $J$ – $V$  characteristics.<sup>[21]</sup> Little or no hysteresis in similar inverted (p–i–n) devices has also been previously reported.<sup>[22,23]</sup> Hysteresis in  $J$ – $V$  curves is a problem for some  $\text{CH}_3\text{NH}_3\text{PbI}_3$  solar cells and has been extensively discussed in the literature,<sup>[24–26]</sup> with slow-moving ion defects in the perovskite being the most likely cause.<sup>[13,27,28]</sup> However, in addition to the slow-moving ions, a strong channel for charge carriers to recombine in the solar cell is also essential to explain the hysteresis.<sup>[14]</sup> Recombination channels do exist in the devices considered in this manuscript which limit their efficiency to 13.2%. It is thus likely that the little hysteresis seen in the experimental devices prepared by some of us<sup>[21]</sup> using vacuum deposition is a result of low ion defect concentration in the perovskite. In our simulations, we find that we do not need to include ions to fit to the experimental data of our devices.

## 2. Results and Discussion

The device structure is p–i–n, where p is the HTL, i is the perovskite absorber layer, and n is the ETL. The devices employ gold (Au) as the cathode and poly(3,4-ethylenedioxythiophene):poly(styrenesulfonic acid) (PEDOT:PSS) and indium tin oxide (ITO) as the anode. The hole transporting material used is poly[*N,N*-bis(4-butylphenyl)-*N,N*-bis(phenyl)benzidine (polyTPD) and the electron transporting material used is [6,6]-phenyl  $\text{C}_{61}$ -butyric acid methylester (PCBM). The perovskite absorber,  $\text{CH}_3\text{NH}_3\text{PbI}_3$ , is deposited by co-evaporating  $\text{PbI}_2$  and  $\text{CH}_3\text{NH}_3\text{I}$  in high vacuum chamber. The perovskite has a band gap ( $E_{\text{gap}}$ ) of 1.55 eV.<sup>[21]</sup> Figure 1 shows the device configuration. Momblona et al.<sup>[21]</sup> reported the influence of the perovskite

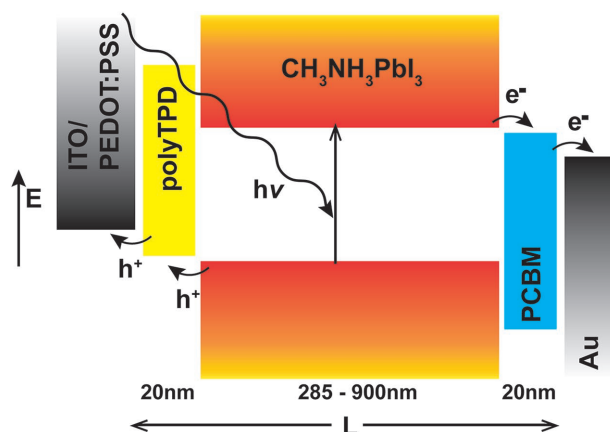


**Figure 1.** Device structure of the perovskite solar cell under study. After illumination, free electrons and holes generated in the perovskite absorber are transported through the respective materials and extracted at the electrodes.

layer thickness on the device performance, with the fill factor (FF) decreasing from 63% for a 285 nm thick device to 40% for a 900 nm thick device. The FF of the 900 nm thick device was recovered to 65% by using a doped-polyTPD (by partial oxidation of polyTPD) as hole transport layer.<sup>[21]</sup> In addition, we also report the light intensity dependence of FF for a 400 nm thick device.<sup>[21]</sup>

We validate our device model by performing a fit to the experimental data using a single set of device parameters which quantitatively explains the thickness dependence, the effect of doping of HTL, and the light intensity dependence of FF.

Our 1D device model is based on the drift-diffusion equations for electrons and holes throughout the device and on solving the Poisson equation in one dimension. The rate of generation of charge carriers is dependent on the absorption profile in the perovskite layer upon illumination of the device and is calculated by using the open source transfer matrix model by Burkhard et al.<sup>[29]</sup> The absorption of light in the perovskite layer is shown to create both excitons and free charges.<sup>[16,30]</sup> However, owing to the low exciton binding energy (a few meV),<sup>[16]</sup> the instantaneous generation of free charges after light absorption in the perovskite is a reasonable assumption in our model. The transport of these free charges is then governed by diffusion and electrically induced drift; for electrons<sup>[31]</sup>

$$J_n(x) = -qn(x)\mu_n \frac{\partial V(x)}{\partial x} + qD_n \frac{\partial n(x)}{\partial x} \quad (1)$$

and for holes

$$J_p(x) = -qp(x)\mu_p \frac{\partial V(x)}{\partial x} - qD_p \frac{\partial p(x)}{\partial x} \quad (2)$$

where  $J_n(x)$  and  $J_p(x)$  are electron and hole current densities respectively,  $q$  is the electronic charge ( $1.602 \times 10^{-19}$  C),  $V(x)$  is the electrostatic potential,  $n(x)$  and  $p(x)$  are electron and hole concentrations,  $\mu_n$  and  $\mu_p$  are electron and hole mobilities and,  $D_n$  and  $D_p$  are electron and hole diffusion constants



respectively. The diffusion constants are assumed to obey the Einstein relation<sup>[31]</sup>

$$D_{n,p} = \mu_{n,p} V_t \quad (3)$$

with  $V_t$  the thermal voltage, i.e.,  $V_t = k_B T/q$ , where  $k_B$  is Boltzmann's constant and  $T$  is the absolute temperature. The position within the device is denoted by  $x$  and represents one spatial dimension. The left contact (between PEDOT:PSS/ITO and polyTPD) is then given by  $x = 0$  and the right contact (between PCBM and Au) by  $x = L$ , where  $L$  is the device thickness.

The electrostatic potential throughout the device is solved from the Poisson's equation

$$\frac{\partial^2}{\partial x^2} V(x) = -\frac{q}{\epsilon(x)} (p(x) - n(x) - N_A^-(x) + N_D^+(x)) \quad (4)$$

with  $\epsilon(x)$  being the permittivity and,  $N_A^-(x)$  and  $N_D^+(x)$  being the ionized p-type and n-type doping, respectively. The doping levels are constant in the ETL and HTL, and zero in the perovskite layer. Henceforth, the  $x$  dependence of variable is dropped for notational convenience and is invoked only occasionally for clarity. The boundary condition on the electrostatic potential is

$$q(V(L) - V(0) + V_{app}) = W_c - W_a \quad (5)$$

where  $V_{app}$  is the externally applied voltage and,  $W_a$  and  $W_c$  are the anode and cathode work functions respectively. The built-in potential is then given by

$$V_{bi} = (W_c - W_a)/q \quad (6)$$

The boundary conditions for charge carriers at electrode contacts are given by Boltzmann statistics; for anode ( $x = 0$ )<sup>[31]</sup>

$$n(0) = N_c \exp\left(-\frac{E_{gap} - \phi_p}{V_t}\right) \quad (7)$$

$$p(0) = N_c \exp\left(-\frac{\phi_p}{V_t}\right) \quad (8)$$

where  $N_c$  is the effective density of states of both the conduction and valence band and  $\phi_p$  is the injection barrier height (in eV) for holes. Similarly, for cathode ( $x = L$ )<sup>[31]</sup>

$$n(L) = N_c \exp\left(-\frac{\phi_n}{V_t}\right) \quad (9)$$

$$p(L) = N_c \exp\left(-\frac{E_{gap} - \phi_n}{V_t}\right) \quad (10)$$

where  $\phi_n$  is the injection barrier height (in eV) for electrons. This denotes that the electrode contacts are in thermodynamic equilibrium, unlike the rest of the device.

The generated charge carriers in  $\text{CH}_3\text{NH}_3\text{PbI}_3$  can recombine via both bimolecular and trap-assisted mechanism. The bimolecular recombination rate ( $R_b$ ) is given by

$$R_b = k_b (np - n_i^2) \quad (11)$$

where  $k_b$  is the bimolecular recombination constant and  $n_i$  is the intrinsic carrier concentration. The trap-assisted recombination rate ( $R_{SRH}$ ) is given by the Shockley–Read–Hall (SRH) equation<sup>[31]</sup>

$$R_{SRH} = \frac{C_n C_p (N_{trap} + P_{trap})}{C_n (n + n_1) + C_p (p + p_1)} (np - n_i^2) \quad (12)$$

where  $N_{trap}$  and  $P_{trap}$  are electron and hole trap concentrations respectively and,  $C_n$  and  $C_p$  are the capture coefficients for electrons and holes respectively. The constants  $n_1$  and  $p_1$  are defined by

$$n_1 = N_c \exp\left(-\frac{E_c - E_{trap}}{k_b T}\right) \quad (13)$$

$$p_1 = N_c \exp\left(-\frac{E_{trap} - E_v}{k_b T}\right) \quad (14)$$

with  $E_{trap}$  being the trap energy in eV. The electron traps ( $N_{trap}$ ) and hole traps ( $P_{trap}$ ) are located in a 5 nm thick interface region between HTL and perovskite and, perovskite and ETL respectively, and operate as recombination centers ( $E_{trap} = E_{gap}/2$ ). Trap-assisted recombination is most effective when the trap is located mid-gap, and is shown to categorically describe the recombination dynamics for an arbitrary distribution of traps near the middle of the band gap as shown in ref. [32]. These interface traps are present in the perovskite absorber layer and have material properties of the perovskite.

To solve the Poisson and continuity equations, Gummel iteration is used. Initially, a guess is made for the carrier densities and potential, and then solving the Poisson equation gives the correction  $\delta V$  to the potential which is subsequently added to the guessed potential. Next, the continuity equations are solved for the carrier densities using the new potential as input. This scheme is iterated until convergence (error is minimized) is reached. To discretize the equations, a finite difference method is used. The total simulation volume is 1000 points leading to a grid spacing ( $\Delta x$ ) of 0.325 nm for the 285 nm thick device and 0.940 nm for the 900 nm thick device. Detailed information about the iteration procedure and the discretization scheme can be found in ref. [33].

**Figure 2a,b** shows the experimental data for  $\text{CH}_3\text{NH}_3\text{PbI}_3$  solar cells with different absorber layer thickness of 285 nm and 900 nm (with and without doped HTL) respectively. The devices are illuminated by a standard AM 1.5G light source. As is evident, the FF decreases significantly with increase in thickness from 285 to 900 nm. Doping of the HTL (polyTPD) in the 900 nm thick device leads to improved efficiency helped by a large gain in FF.<sup>[21]</sup> Now, we perform simulations and fit the simulated data to the experimental data, and we achieve this

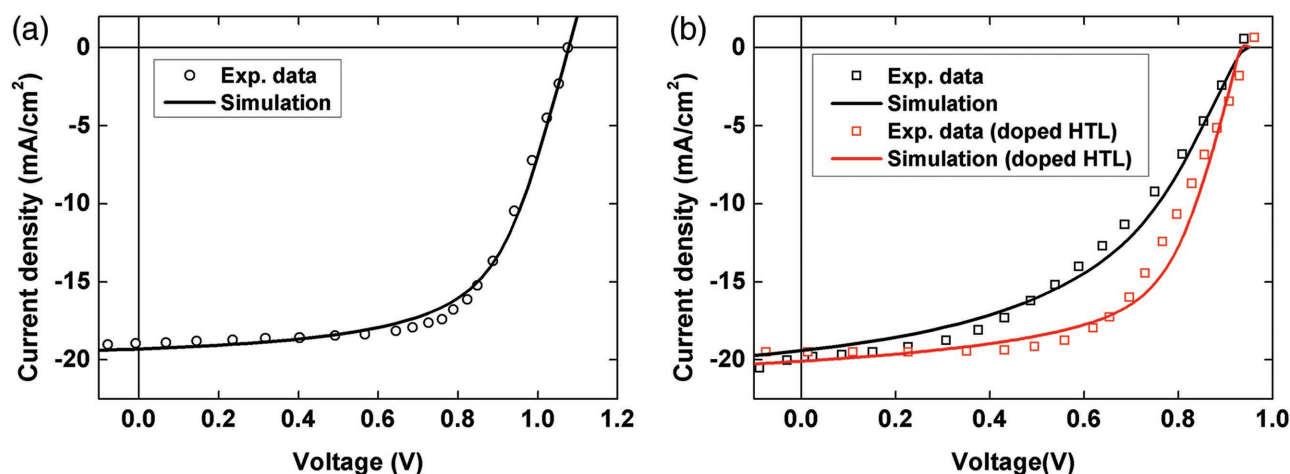


**Figure 2.**  $J$ - $V$  characteristics of perovskite solar cells with absorber thickness of a) 285 nm with undoped hole transport layer (HTL), and b) 900 nm with undoped and doped HTL. The open symbols in both plots are experimental data obtained from ref. [21] for  $\text{CH}_3\text{NH}_3\text{PbI}_3$  solar cells. The solid line represents the simulations. Note the change in scale at the bottom in (b) as compared to (a).

by using only a single set of device parameters as input to our device model.

A fit to the experimental data is shown in Figure 2 for both 285 and 900 nm thick devices. We find that we need weak bimolecular recombination in the perovskite bulk and trap-assisted recombination at interfaces to fit the simulation to the experimental data. In addition, we also find that we do not need to include ions to fit to the experimental data. The calculated charge carrier generation profile throughout the device after illumination is depicted in Figure 3. The optical constants ( $\eta$ ,  $\kappa$ ) of the all materials used are obtained from the literature and are listed in Table S1 in the Supporting Information. Table 1 provides an overview of the device parameters used in the simulation. The electron and hole mobilities in  $\text{CH}_3\text{NH}_3\text{PbI}_3$  are extracted from the fit and are in good agreement with values ( $10^{-4}$ – $10$   $\text{cm}^2 \text{Vs}^{-1}$ ) reported in the literature.<sup>[17,34–36]</sup> The perovskite bimolecular recombination coefficient extracted from the fit is also in good agreement with reported values ( $2 \times 10^{-11}$  to  $5 \times 10^{-9}$   $\text{cm}^3 \text{s}^{-1}$ ).<sup>[17,20,37]</sup> The maximum generation rate is fit to

match the short-circuit current density of the 285 nm thick and 900 nm thick device. The HTL/perovskite and perovskite/ETL interface traps account for the open grain boundaries that are invariably present at material interfaces which can cause the charge carriers to recombine nonradiatively. As the perovskite is grown by evaporation on the HTL surface during preparation of all devices, the quality of the HTL/perovskite interface remains unchanged for devices of all thicknesses. However, the perovskite/ETL interface changes with increasing perovskite growth times and device thickness. We therefore fix the HTL/perovskite interface trap density ( $P_{\text{trap}}$ ) to  $2.5 \times 10^9 \text{ cm}^{-2}$  for devices with all thicknesses. The perovskite/ETL interface trap density ( $N_{\text{trap}}$ ) is  $1.5 \times 10^9 \text{ cm}^{-2}$  for the 285 nm thick device and  $1.5 \times 10^{11} \text{ cm}^{-2}$  for the 900 nm thick device. A fit to the experimental data (light intensity dependence of FF) of the 400 nm thick device (shown in Figure 4) gives  $N_{\text{trap}}$  of  $5 \times 10^{10} \text{ cm}^{-2}$ . As can be seen from Figure 2 and Figure 4, using a single set of device parameters, we see excellent agreement between experimental and simulated data, including the influence of the device thickness, the doping of HTL and the light intensity dependence of FF.

We note that the carrier mobility in the perovskite extracted from the fit is at the lower end of the literature values spectrum.<sup>[17,34–36]</sup> However, when the perovskite mobility was set to lower value ( $\leq 10^{-2} \text{ cm}^2 \text{Vs}^{-1}$ ) in simulations, there was no significant increase in FF with HTL doping (Figure 2b) as seen in experiments, stating that this mobility value (of perovskite) is too low for efficient charge transport despite the increase in electric field strength in the perovskite due to HTL doping. Here, the doping of HTL increases its conductivity by increasing the equilibrium hole density in the layer. We assume that the hole mobility in HTL is unchanged after doping. On the other hand, simulation results with higher value ( $\geq 10^{-1} \text{ cm}^2 \text{Vs}^{-1}$ ) of perovskite mobilities could not explain the large decrease in FF (63% to 40%)<sup>[21]</sup> as the absorber thickness is increased from 285 nm to 900 nm, suggesting that this mobility value (of perovskite) is too high to quench charge transport in the 900 nm thick device. We also performed simulations with traps/defects in the perovskite bulk, but the simulated data did not fit the experimental

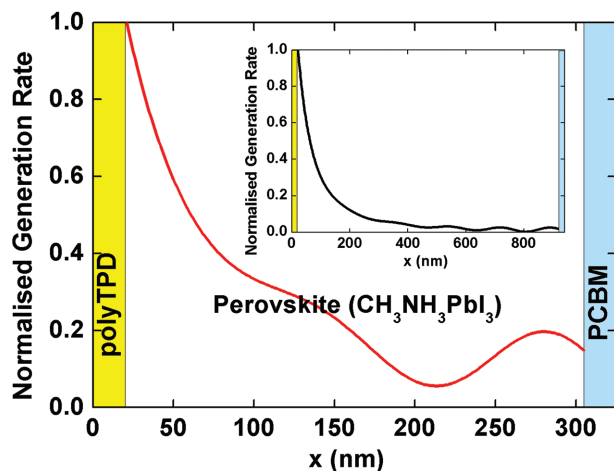


**Figure 3.** Normalized generation rate of charge carriers throughout the 285 nm thick and 900 nm thick (inset graph) device as calculated by using the transfer matrix model.<sup>[29]</sup>

**Table 1.** Parameters used in the device simulation to obtain the fit, including the ones from the literature.

Parameter	Symbol	Value	
Perovskite band gap	$E_{\text{gap}}$	1.55 eV	Ref. [21]
Density of states (DOS)	$N_c$	$8.1 \times 10^{18} \text{ cm}^{-3}$	Ref. [38]
Perovskite conduction band minimum	$E_c$	−5.43 eV	Ref. [10]
Perovskite valence band maximum	$E_v$	−3.88 eV	Ref. [10]
polyTPD HOMO level	$E_{\text{HOMO}}$	−5.4 eV	Ref. [10]
PCBM LUMO level	$E_{\text{LUMO}}$	−3.9 eV	Ref. [10]
Built-in voltage at short-circuit	$V_{\text{bi}}$	1.1 V	Ref. [21]
Hole mobility in polyTPD (HTL)	$\bar{\mu}_p$	$1 \times 10^{-3} \text{ cm}^2 \text{ Vs}^{-1}$	Ref. [39]
Electron mobility in PCBM (ETL)	$\bar{\mu}_n$	$2 \times 10^{-3} \text{ cm}^2 \text{ Vs}^{-1}$	Ref. [40]
Perovskite relative permittivity	$\epsilon$	24.1	Ref. [38]
polyTPD relative permittivity	$\epsilon_p$	3	
PCBM relative permittivity	$\epsilon_n$	3.9	Ref. [40]
Electron and hole capture coefficients	$C_{n,p}$	$1 \times 10^{-13} \text{ m}^3 \text{ s}^{-1}$	Ref. [41]
Electron and hole mobility in perovskite	$\mu_n, \mu_p$	$5 \times 10^{-2} \text{ cm}^2 \text{ Vs}^{-1}$	Fit
Maximum charge generation rate	$G_{\text{max}}$	$7.51 \times 10^{21} \text{ cm}^{-3} \text{ s}^{-1}$	Fit
Bimolecular recombination constant	$k_b$	$6 \times 10^{-11} \text{ cm}^3 \text{ s}^{-1}$	Fit
HTL/perovskite interface trap density	$P_{\text{trap}}$	$2.5 \times 10^9 \text{ cm}^{-2}$	Fit
Perovskite/ETL interface trap density	$N_{\text{trap}}$	$1.5 \times 10^9$ – $1.5 \times 10^{11} \text{ cm}^{-2}$	Fit
Ionized doping in PCBM	$N_D^+$	$1 \times 10^{14} \text{ cm}^{-3}$	Fit
Ionized doping in polyTPD	$N_A^-$	$1 \times 10^{15} \text{ cm}^{-3}$	Fit
Number of grid points		1000	
Grid spacing	$\Delta x$	0.325–0.940 nm	

data using a single set of device parameters and also failed to explain all the experimental observations exhaustively viz. thickness dependence, effect of doping of HTL and light intensity dependence of FF. The recovery of FF (increase from 40% to 60%) after doping of the HTL is an evidence of the high quality of the perovskite bulk absorber deposited by vacuum co-evaporation.<sup>[21]</sup> This illustrates the high diffusion lengths of charge

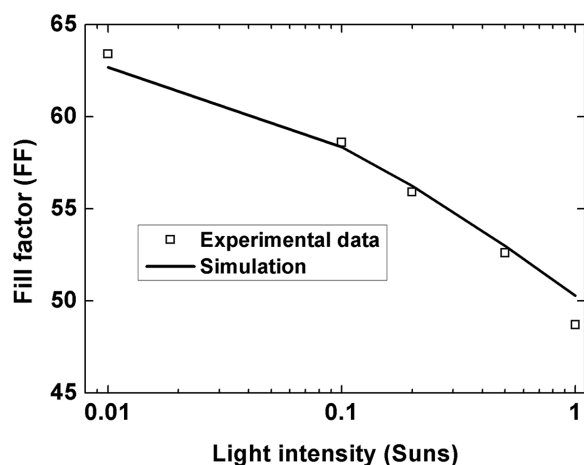


**Figure 4.** Fill factor of 400 nm thick device at different light intensities. The open squares represent experimental data and the solid line denotes the simulation. 1 sun = 100 mW cm<sup>−2</sup>.

carriers and the presence of low defect (or trap) density in the perovskite bulk, strengthening our premise of traps (or recombination centers) at interfaces only.

After validation of our model we can now analyze the device behavior in detail. The electric potential, current densities and carrier densities for the 285 nm thick device under short-circuit (SC) conditions ( $V_{\text{app}} = 0 \text{ V}$ ) are depicted in **Figure 5a,b**. The low dielectric nature of the organic materials employed as HTL and ETL results in a significant potential drop across these transport layers. The electric field in the perovskite layer is constant except at the interfaces with transport layers where the permittivity function,  $\epsilon(x)$ , changes abruptly. As a consequence of the non-uniform generation of charge carriers (shown in **Figure 3**), current densities exhibit a non-linear dependence on position despite the constant electric field in the perovskite bulk. In the transport layers however, the current densities are constant since the majority carrier density (electron in ETL and hole in HTL) is significantly higher than the minority carrier density (hole in ETL and electron in HTL) and bimolecular recombination is very low. The charge densities are high at the contacts ( $x = 0$  and  $x = L$ ) but fall rapidly in the thin transport layers, owing to the presence of the strong electric field and the low conductivity of the organic materials.

The nonuniform generation profile also results in electron density to be higher than the hole density in the perovskite bulk, notwithstanding their balanced mobilities. When in SC, only 3.7% of the generated charge carriers recombine (**Table 2**)

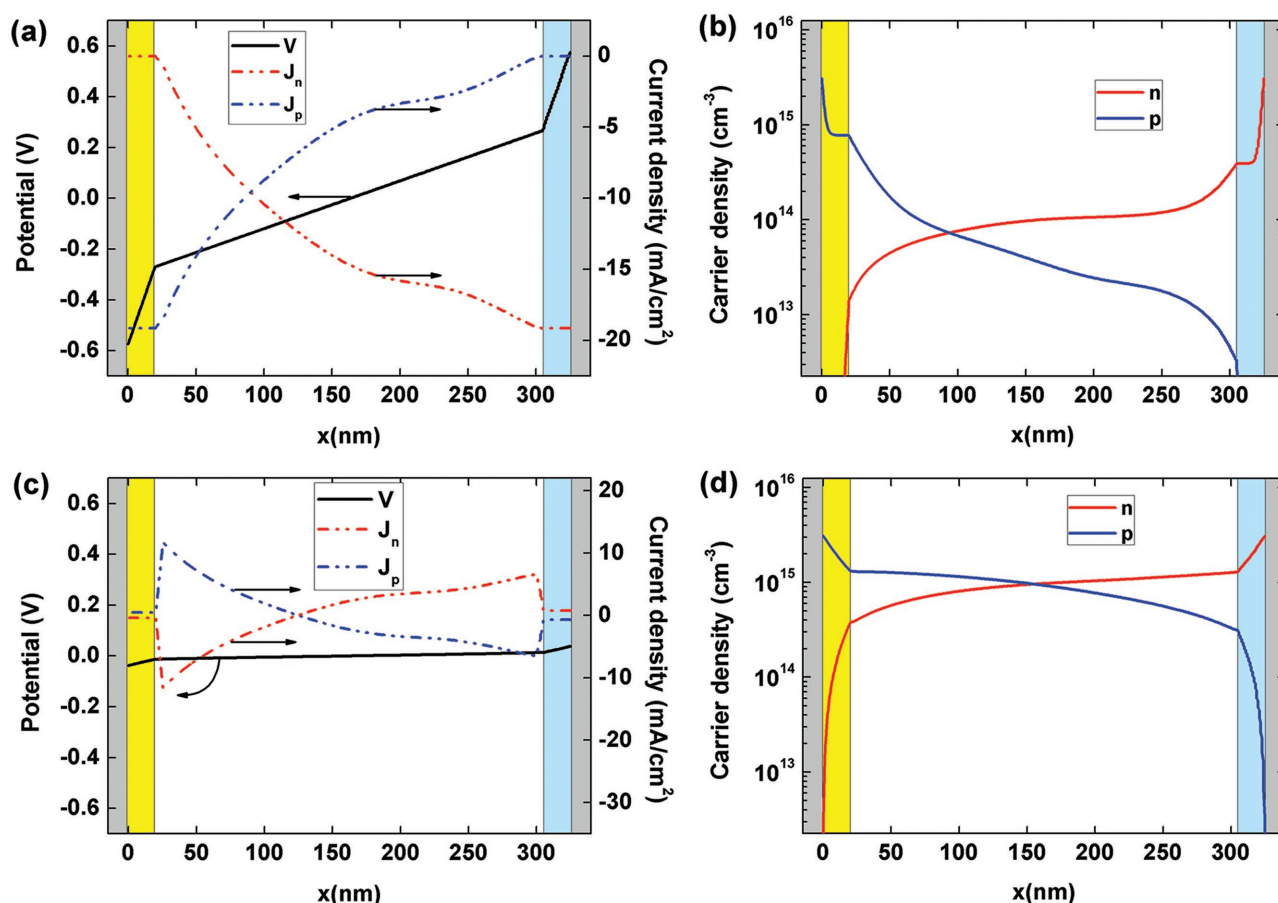


**Figure 5.** Potential, current densities and carrier densities at a, b) short-circuit and c, d) open-circuit conditions for the 285 nm thick device. The background colors show different device stacks with (from left to right) ITO/PEDOT:PSS, HTL (yellow), perovskite, ETL (blue), and Au. Note the change in scale on the right hand side in (c) as compared to (a).

and the rest are extracted efficiently. This is a consequence of the high charge carrier mobilities (as compared to organic layers) in perovskite, despite only a modest electric field ( $\approx 1.85 \times 10^6 \text{ V m}^{-1}$ ) in the perovskite bulk. The charge extraction efficiency is lower in the 900 nm thick device as compared to the 285 nm thick device as the electric field is weaker in the thicker device and therefore, despite stronger light absorption in the 900 nm thick device, only a marginal increase in  $J_{\text{SC}}$  is realized. Bimolecular recombination, which is proportional to the product of carrier densities, is low as the carrier densities in the perovskite are low ( $\approx 10^{13}$ – $10^{14} \text{ cm}^{-3}$ ) resulting in the dominant loss mechanism being SRH recombination.

Figure 5d shows the potential, current densities and charge densities under open-circuit (OC) conditions ( $V_{\text{app}} = V_{\text{OC}}$ ). As

compared to SC, the electric field is very small in the device. There is an equilibrium between drift and diffusion of charge carriers which results in net zero current densities in the device. With only a weak electric field to help charge extraction, the carrier densities are high as compared to SC. This results in recombination of all of the generated charge carriers in the perovskite bulk.

Just as in OC and SC conditions, SRH recombination is the dominant recombination mechanism when the device is operating at maximum power (MP), with overall carrier recombination being 22% of all generated carriers. As a solar cell is operated at MP, the pathways leading to SRH recombination in perovskite solar cell need to be addressed. Surface recombination occurs when charge carriers reach the

**Table 2.** Voltage, current density and, total recombination loss at short-circuit (SC), maximum power (MP) and open-circuit (OC) conditions. Total recombination is divided into bimolecular, SRH and surface recombination.

	$V_{\text{app}}$ [V]	$J$ [ $\text{mA cm}^{-2}$ ]	Total recombination [%]	Bimolecular recombination [%]	SRH (at interface) recombination [%]	Surface recombination [%]
SC	0	19.0	3.7	0.2	99.8	0
MP	0.81	15.4	22	0.7	99.2	0.1
OC	1.07	0	100	1.4	92.8	5.8

wrong electrodes (ITO/PEDOT:PSS for electrons and Au for holes) and recombine with the majority carriers at the respective electrodes. The surface of the perovskite is covered with transport layer forming an interface, where SRH recombination is dominant as discussed in this paper. Our results are in line with Yang et al.<sup>[42]</sup> who report significant recombination at the perovskite surface. From Table 2, surface recombination at electrodes is significantly lower than interface SRH recombination, implying that surface recombination at the electrodes is not a major recombination process in perovskite solar cells.

Having discussed the device behavior in detail, we now explore ways to increase the device performance of perovskite solar cells. One such method involves the doping of polyTPD (HTL) to increase the FF from 40% to 65%.<sup>[21]</sup> Our model is able to reproduce this experimental result and shows excellent agreement as is depicted in Figure 2b. Doping of polyTPD increases the equilibrium carrier density in the layer increasing its conductivity which results in a lower drop in potential across the polyTPD (Figure S1 in the Supporting Information). This results in a stronger electric field in the perovskite bulk giving

rise to increased charge extraction and lower recombination which is reflected in the increase in FF.

The influence of the charge carrier mobilities on the device performance is shown in Figure 6a. Increase in mobility results in faster extraction of charge carriers which reduces the carrier density in the perovskite bulk leading to low carrier recombination. This is reflected in a higher FF and  $J_{SC}$  leading to PCE up to 16.8%. As the electric field strength in the perovskite layer is unchanged, there is no influence on the  $V_{OC}$ .

The presence of energetic barriers at contacts for charge injection/extraction can play a detrimental role on device performance as can be seen in Figure 6b. As shown in Equation (6), lowering of the energetic barriers (by modifying the work-functions of contacts) gives rise to increased device built-in potential ( $V_{bi}$ ) and this leads to higher  $V_{OC}$ . The increase in electric field strength results in faster charge extraction and an increase in FF. The magnitude (height) of the energetic barriers is dependent on the choice of electrodes and transport layers having different work-functions and band gaps. Mitigation of these barriers by careful choice of materials is essential for increasing device efficiency.

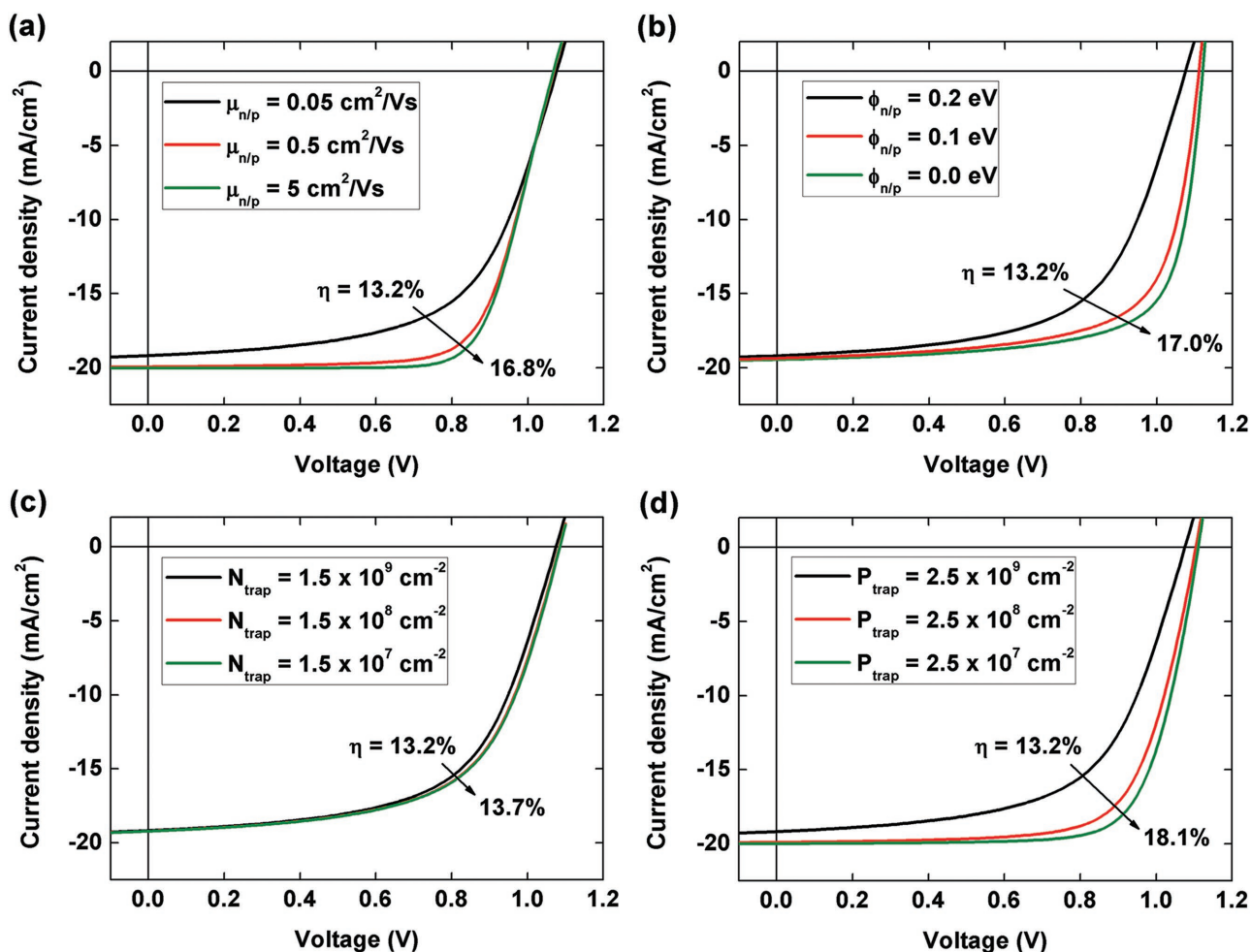


**Figure 6.** Simulated  $J$ - $V$  curves for different a) carrier mobilities, b) injection barriers, c) electron trap density at ETL/perovskite interface, and d) hole trap density at perovskite/HTL interface. The black line in every subfigure follows the experimental data from Figure 2.



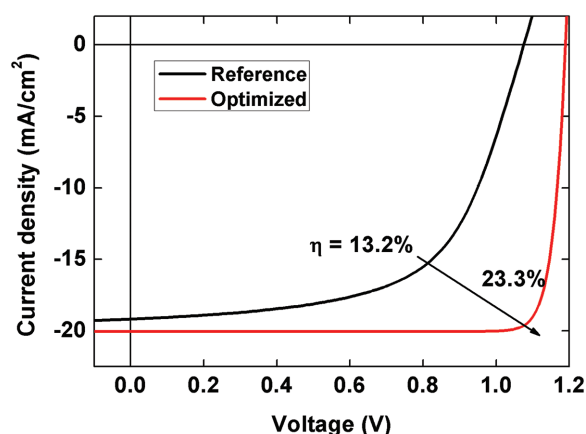


**Figure 7.** Simulated  $J$ - $V$  curve (red) for the optimized perovskite solar cell.

From Table 2, SRH recombination via traps or defects is the dominant recombination mechanism during device operation. The influence of passivation of traps located at the interface between the perovskite and the transport layers is shown in Figure 6c,d. As can be seen from the figures, the quality of the HTL/perovskite (front) interface has a far greater impact on the device characteristics as compared to the perovskite/ETL (back) interface. This is because the solar cell is illuminated from the HTL side resulting in higher concentration of free charge carriers near the HTL/perovskite interface as is clear from the generation profile shown in Figure 3. Higher concentration of free charge carriers means there are excess of generated electrons available for recombination with trapped holes at the HTL/perovskite front interface. The efficiency of the perovskite solar cell jumps significantly (13.2% to 18.1%, an increase of 40%) with passivation of traps, emphasizing the need to address interface SRH recombination loss (especially at the front interface).

An optimized device with increased carrier mobilities, reduced energetic barriers and, passivated traps can lead to PCE of 23.3% having superior FF and  $V_{OC}$  as shown in Figure 7. This is however, by no means the upper limit (theory or practical) to the efficiency. Here, the optimized device has a thickness of 285 nm which limits the  $J_{SC}$  of the solar cell around  $20 \text{ mA cm}^{-2}$  whereas, the current state-of-the-art perovskite solar cells are 450–550 nm thick and show  $J_{SC}$  approaching  $23 \text{ mA cm}^{-2}$ .<sup>[8,43]</sup> Increasing the perovskite absorber thickness should further increase the cell performance, with a PCE beyond 25% realizable.

### 3. Conclusion

We have developed and validated a device model for the operation of perovskite solar cells (PSCs). The model quantitatively explained the role of contacts, the electron and hole transport layers, charge generation, drift and diffusion of charge carriers and recombination. The model was used to simulate experimental data of vacuum deposited p-i-n perovskite ( $\text{CH}_3\text{NH}_3\text{PbI}_3$ ) solar cells made by some of us.<sup>[21]</sup> Excellent agreement was found between simulated and experimental data over multiple device thicknesses, including the doping of

HTL and the light intensity dependence of FF. Trap-assisted recombination at interfaces was found to be the dominant recombination mechanism at short-circuit, maximum power, and open-circuit conditions. Mitigation of interface recombination by passivation of traps was shown to increase the device PCE by 40%, emphasizing the need to address trap-assisted recombination (especially at the front HTL/perovskite interface) channels in perovskite solar cells. The optimization of 285 nm thick  $\text{CH}_3\text{NH}_3\text{PbI}_3$  solar cell resulted in PCE of 23.3%, with a target of 25% realizable by increasing the perovskite absorber thickness.

### Supporting Information

Supporting Information is available from the Wiley Online Library or from the author.

### Acknowledgements

T.S.S. would like to thank V.M. Le Corre, University of Groningen for fruitful discussions and assistance with using the transfer matrix model. The Valencian team acknowledges support from the Spanish Ministry of Economy and Competitiveness (MINECO) via the Unidad de Excelencia Mara de Maeztu MDM-2015-0538, MAT2014-55200, and PCIN-2015-255, and the Generalitat Valenciana (Prometeo/2016/135). C.M. thanks MINECO Spain for their pre-doctoral contract.

This work is part of the Industrial Partnership Programme (IPP) “Computational sciences for energy research” of the Foundation for Fundamental Research on Matter (FOM), which is part of the Netherlands Organisation for Scientific Research (NWO). This research program is cofinanced by Shell Global Solutions International B.V. This is a publication by the FOM Focus Group “Next Generation Organic Photovoltaics”, participating in the Dutch Institute for Fundamental Energy Research (DIFFER). The authors declare no competing financial interest.

Received: November 3, 2016

Revised: December 16, 2016

Published online: February 21, 2017

- [1] NREL Best Research-Cell Efficiencies. [http://www.nrel.gov/ncpv/images/efficiency\\_chart.jpg](http://www.nrel.gov/ncpv/images/efficiency_chart.jpg), accessed: December, 2016.
- [2] A. Kojima, K. Teshima, Y. Shirai, T. Miyasaka, *J. Am. Chem. Soc.* **2009**, *131*, 6050.
- [3] S. D. Stranks, G. E. Eperon, G. Grancini, C. Menelaou, M. J. Alcocer, T. Leijtens, L. M. Herz, A. Petrozza, H. J. Snaith, *Science* **2013**, *342*, 341.
- [4] E. Edri, S. Kirmayer, S. Mukhopadhyay, K. Gartsman, G. Hodes, D. Cahen, *Nat. Commun.* **2014**, *5*, 3461.
- [5] L. Meng, J. You, T.-F. Guo, Y. Yang, *Acc. Chem. Res.* **2015**, *49*, 155.
- [6] T. M. Brenner, D. A. Egger, L. Kronik, G. Hodes, D. Cahen, *Nat. Rev. Mater.* **2016**, *1*, 15007.
- [7] J. You, Z. Hong, Y. M. Yang, Q. Chen, M. Cai, T.-B. Song, C.-C. Chen, S. Lu, Y. Liu, H. Zhou, Y. Yang, *ACS Nano* **2014**, *8*, 1674.
- [8] W. Nie, H. Tsai, R. Asadpour, J.-C. Blancon, A. J. Neukirch, G. Gupta, J. J. Crochet, M. Chhowalla, S. Tretiak, M. A. Alam, H.-L. Wang, A. D. Mohite, *Science* **2015**, *347*, 522.
- [9] M. Liu, M. B. Johnston, H. J. Snaith, *Nature* **2013**, *501*, 395.
- [10] O. Malinkiewicz, A. Yella, Y. H. Lee, G. M. Espallargas, M. Graetzel, M. K. Nazeeruddin, H. J. Bolink, *Nat. Photonics* **2014**, *8*, 128.

- [11] E. Wei, X. Ren, L. Chen, W. C. Choy, *Appl. Phys. Lett.* **2015**, *106*, 221104.
- [12] A. Walsh, *J. Phys. Chem. C* **2015**, *119*, 5755.
- [13] G. Richardson, S. E. O'Kane, R. G. Niemann, T. A. Peltola, J. M. Foster, P. J. Cameron, A. B. Walker, *Energy Environ. Sci.* **2016**, *9*, 1476.
- [14] S. van Reenen, M. Kemerink, H. J. Snaith, *J. Phys. Chem. Lett.* **2015**, *6*, 3808.
- [15] T. Minemoto, M. Murata, *J. Appl. Phys.* **2014**, *116*, 054505.
- [16] A. Miyata, A. Mitoglu, P. Plochocka, O. Portugall, J. T.-W. Wang, S. D. Stranks, H. J. Snaith, R. J. Nicholas, *Nat. Phys.* **2015**, *11*, 582.
- [17] C. Wehrenfennig, G. E. Eperon, M. B. Johnston, H. J. Snaith, L. M. Herz, *Adv. Mater.* **2014**, *26*, 1584.
- [18] G. A. H. Wetzelaer, M. Scheepers, A. M. Sempere, C. Momblona, J. Ávila, H. J. Bolink, *Adv. Mater.* **2015**, *27*, 1837.
- [19] M. B. Johnston, L. M. Herz, *Acc. Chem. Res.* **2015**, *49*, 146.
- [20] J.-C. Blancon, W. Nie, A. J. Neukirch, G. Gupta, S. Tretiak, L. Cognet, A. D. Mohite, J. J. Crochet, *Adv. Funct. Mater.* **2016**, *26*, 4283.
- [21] C. Momblona, O. Malinkiewicz, C. Roldán-Carmona, A. Soriano, L. Gil-Escrig, E. Bandiello, M. Scheepers, E. Edri, H. J. Bolink, *APL Mater.* **2014**, *2*, 081504.
- [22] Y. Shao, Z. Xiao, C. Bi, Y. Yuan, J. Huang, *Nat. Commun.* **2014**, *5*, 5784.
- [23] J. H. Heo, H. J. Han, D. Kim, T. K. Ahn, S. H. Im, *Energy Environ. Sci.* **2015**, *8*, 1602.
- [24] H. J. Snaith, A. Abate, J. M. Ball, G. E. Eperon, T. Leijtens, N. K. Noel, S. D. Stranks, J. T.-W. Wang, K. Wojciechowski, W. Zhang, *J. Phys. Chem. Lett.* **2014**, *5*, 1511.
- [25] E. L. Unger, E. T. Hoke, C. D. Bailie, W. H. Nguyen, A. R. Bowring, T. Heumüller, M. G. Christoforo, M. D. McGehee, *Energy Environ. Sci.* **2014**, *7*, 3690.
- [26] W. Tress, N. Marinova, T. Moehl, S. M. Zakeeruddin, M. K. Nazeeruddin, M. Grätzel, *Energy Environ. Sci.* **2015**, *8*, 995.
- [27] C. Eames, J. M. Frost, P. R. Barnes, B. C. Oregan, A. Walsh, M. S. Islam, *Nat. Commun.* **2015**, *6*, 7497.
- [28] S. Meloni, T. Moehl, W. Tress, M. Franckevičius, M. Saliba, Y. H. Lee, P. Gao, M. K. Nazeeruddin, S. M. Zakeeruddin, U. Rothlisberger, M. Graetzel, *Nat. Commun.* **2016**, *7*, 10334.
- [29] G. F. Burkhard, E. T. Hoke, M. D. McGehee, *Adv. Mater.* **2010**, *22*, 3293.
- [30] Q. Lin, A. Armin, R. C. R. Nagiri, P. L. Burn, P. Meredith, *Nat. Photonics* **2014**, *3*, 106.
- [31] S. Selberherr, *Analysis and Simulation of Semiconductor Devices*, Springer-Verlag, Vienna **1984**.
- [32] J. Simmons, G. Taylor, *Phys. Rev. B* **1971**, *4*, 502.
- [33] L. J. A. Koster, E. C. P. Smits, V. D. Mihailetschi, P. W. M. Blom, *Phys. Rev. B* **2005**, *72*, 085205.
- [34] B. Maynard, Q. Long, E. A. Schiff, M. Yang, K. Zhu, R. Kottokaran, H. Abbas, V. L. Dalal, *Appl. Phys. Lett.* **2016**, *108*, 173505.
- [35] Y. Chen, J. Peng, D. Su, X. Chen, Z. Liang, *ACS Appl. Mater. & Interfaces* **2015**, *7*, 4471.
- [36] N. Ahn, D.-Y. Son, I.-H. Jang, S. M. Kang, M. Choi, N.-G. Park, *J. Am. Chem. Soc.* **2015**, *137*, 8696.
- [37] D. W. De Quilettes, S. M. Vorphal, S. D. Stranks, H. Nagaoka, G. E. Eperon, M. E. Ziffer, H. J. Snaith, D. S. Ginger, *Science* **2015**, *6*, 7961.
- [38] F. Brivio, K. T. Butler, A. Walsh, M. Van Schilfgaarde, *Phys. Rev. B* **2014**, *89*, 155204.
- [39] S. Cheylan, J. Puigdollers, H. J. Bolink, E. Coronado, C. Voz, R. Icbilla, G. J. Badenes, *J. Appl. Phys.* **2008**, *103*, 096110.
- [40] V. D. Mihailetschi, J. K. Van Duren, P. W. M. Blom, J. C. Hummelen, R. A. Janssen, J. M. Kroon, M. C. Rispen, W. J. H. Verhees, M. M. Wienk, *Adv. Funct. Mater.* **2003**, *13*, 43.
- [41] S. Shao, M. Abdu-Aguye, T. S. Sherkar, H.-H. Fang, S. Adjokatse, G. T. Brink, B. J. Kooi, L. J. A. Koster, M. A. Loi, *Ad. Funct. Mater.* **2016**, *26*, 8094.
- [42] Y. Yang, Y. Yan, M. Yang, S. Choi, K. Zhu, J. M. Luther, M. C. Beard, *Nat. Commun.* **2015**, *6*, 7961.
- [43] H. Zhou, Q. Chen, G. Li, S. Luo, T.-B. Song, H.-S. Duan, Z. Hong, J. You, Y. Liu, Y. Yang, *Science* **2014**, *345*, 542.